Electron cyclotron current drive calculated for ITER conditions using different models

N.B. Marushchenko, H. Maassberg, Yu. Turkin

Max-Planck-Institut für Plasmaphysik, EURATOM-Association, Greifswald, Germany

E-mail: nikolai.marushchenko@ipp.mpg.de

Abstract. The current drive efficiency for the ITER reference Scenario-2 has been calculated by the newly developed ray-tracing code TRAVIS for both the upper and equatorial launcher. For comparison, two adjoint approach models are applied, the high-speed-limit model and a model with the parallel momentum conservation taken into account. It is shown, that in the angle range expected as optimal launch angles the momentum conservation correction produces a non-negligible contribution in ECCD, leading to the necessity to revise the previous predictions carefully. Additionally, the scenario with reduced magnetic field is checked. It is shown, that the ECCD efficiency (as well as the deposition profile) for the equatorial launcher may significantly be changed due to unwanted absorption at the higher (parasitic) harmonics.

PACS numbers: 52.25Xz, 52.35Hr, 52.50Sw, 52.55Wq

1. Introduction

Oblique launch of RF power is an effective tool for both heating (ECRH) and current drive (ECCD), and is an important component of the ITER project [1]. Due to its highly localized deposition profile and relatively simple angle steering, ECCD is planned to sustain the plasma current at the level necessary for high performance and to control the most dangerous magnetohydrodynamic instabilities like the neoclassical tearing mode (NTM) at $q = 3/2$ and $q = 2$, as well the sawtooth instability at $q = 1$. For these tasks two different launchers are designed [2]: the equatorial launcher (it contains three mirrors, situated at the top, middle and bottom of the port) for on/off axis heating and current drive, and the upper launcher for stabilizing of NTM. The chosen frequency is 170 GHz, and the total power which can be launched from the different ports is 20 MW.

Optimal launch angles depend on the scenario and on the task to be performed and have been studied intensively [2, 3, 4]. This was done with help of different ray/beam-tracing codes, which are well benchmarked against each other. Nevertheless, for some cases the current drive efficiency calculated by Fokker-Planck simulations is different from predictions of the ray/beam-tracing codes with the adjoint approach implemented [5, 6].

One from the most important points for current drive calculation with help of the adjoint approach is the choice of the model for the corresponding Spitzer function (solution of the Spitzer-Härm problem). The most common is the "high-speed-limit" [8, 9] (below abbreviated as hsl-model), where the Spitzer function is calculated in the model which does not conserve the parallel momentum of electrons for electron-electron collisions, thereby omitting the transfer of momentum to the bulk electrons and their contribution in the parallel electron flow. Strictly speaking, the linearized collision operator needed for solving the Spitzer-Härm problem is simplified by i) using the diffusion coefficient in the high-speed-limit, and ii) omitting its integral part. (Note, that the simplified approach used by Cohen [8] is, in fact, a further simplification, based on the asymptotic formulation of the hsl-model for $p/p_{\rm th} \gg 1$, and the additional approximation of the magnetic field as the square magnetic well.) The hsl-model (especially the model of Cohen) is truly applicable only for scenarios with sufficiently large launch angles in an optically thick plasma, where bulk electrons are not involved in the cyclotron interaction. At the same time, for the scenarios where electrons with $p/p_{\rm th} \sim 1$ are mainly responsible for absorption and/or the number of trapped particles in the heated area is quite small, the current calculated in the high-speed limit approach may differ from the Fokker-Planck results for some cases by a factor of about two.

A relatively simple numerical algorithm for the Spitzer function calculation with momentum conservation taken into account (mc-model) has been developed [10]. This model was initially implemented in the old IPP W7-AS ray-tracing code and applied for estimations of the ECCD efficiency in the W7-X stellarator [10]. The main advantage of the mc-model, based on the variational principle [11] with the specific collisional operator [12], is the more accurate calculation of the ECCD efficiency, the value of which

is quite close to the result of Fokker-Planck simulation. Being adapted to the relativistic variables, this model is implemented also in the new ray-tracing code TRAVIS [13, 14]. The hsl-model, which is also used in the present paper, is almost the same as formulated in Ref. [9]. The geometrical factor being common for both hsl- and mc-model is defined for arbitrary 3D magnetic configurations, i.e. without the tokamak symmetry assumed.

In the present work, we report the results of angle scans for both upper and equatorial launchers, which are performed with the TRAVIS code. Additionally, the scenario with reduced magnetic field is considered, where the contribution of higher harmonics is estimated. The plasma profiles and the magnetic configuration correspond to the ITER reference Scenario-2 [15] with $Q = 10$, $I_p = 15$ MA, $n_{e0} = 1.02 \times 10^{20}$ m^{-3}, $T_{e0} = 24.8$ keV. Start positions and divergence for each beam are the same as defined in [3].

2. Description of the TRAVIS code

The new ray tracing code TRAVIS [13, 14] (TRAcing VISualized) was developed for electron cyclotron studies in arbitrary 3D magnetic configurations, with emphasis on heating, current drive (CD) and ECE diagnostics. The 3D magnetic configuration is converted to Boozer co-ordinates and interpolated by a highly optimized package. The code is controlled by means of a graphical user interface, which allows the preparation of input parameters and viewing the results in convenient (2D and 3D) form. The aim of this interface is to make the code suitable for any interested user.

The ray tracing equations are the standard Hamiltonian ones (see, e.g. [16]),

$$\frac{d\mathbf{r}}{ds} = \frac{\partial \mathcal{H}}{\partial \mathbf{N}} \cdot \left| \frac{\partial \mathcal{H}}{\partial \mathbf{N}} \right|^{-1}, \quad \frac{d\mathbf{N}}{ds} = -\frac{\partial \mathcal{H}}{\partial \mathbf{r}} \cdot \left| \frac{\partial \mathcal{H}}{\partial \mathbf{N}} \right|^{-1}, \tag{1}$$

where $\mathbf{r}$ is the radius-vector, $\mathbf{N} = \mathbf{k}c/\omega$ is the refractive index vector, and s is the path along the ray. For the Hamiltonian, $\mathcal{H}$, the most general form suggested by Tokman and Westerhof [17] (which includes an "anomalous" dispersion effect) is adopted:

$$\mathcal{H} = \Re \left(e_i^* D_{ij}^H e_j \right), \tag{2}$$

where $D_{ij}^H = N^2 \delta_{ij} - N_i N_j - \epsilon_{ij}^H$, and $\mathbf{e} = \mathbf{E}/E$ is the mode polarization vector calculated as eigenvector of the wave dispersion equation with the full dielectric tensor, $\epsilon_{ij} = \epsilon_{ij}^H + i\epsilon_{ij}^{aH}$, taken in the weakly relativistic approach. Electron cyclotron absorption is calculated through the general formulation (see, e.g. Ref. [18]),

$$\alpha_{\rm ec} = \pi \frac{\omega}{c} \frac{e_i^* \varepsilon_{ij}^{aH} e_j}{|\mathbf{F}(\omega, \mathbf{N})|}, \qquad \mathbf{F}(\omega, \mathbf{N}) = \frac{1}{2} \frac{\partial}{\partial \mathbf{N}} \Re \left(e_i^* D_{ij}^H e_j \right), \tag{3}$$

with the anti-hermitian part of the dielectric tensor, ε_{ij}^{aH}, taken in a fully relativistic approach. Normalized by $cE^2/8\pi$ the power flux density, $\mathbf{F}(\omega, \mathbf{N})$, corresponds to the Tokman-Westerhof model [17], and, in some sense, can be used also as definition of the group velocity, $\mathbf{v}_{\rm gr} = c\,\mathbf{F}$, with the absolute value not exceeding the speed of light even in the vicinity of the resonances. Please, note, that we apply two different definitions for the

dielectric tensor: ϵ_{ij}, which is used for calculation of D_{ij}^H, of the polarization, $\mathbf{e}$, and of the power flux, $\mathbf{F}$, is taken in the weakly relativistic approach, sufficient for describing the wave propagation physics; and ε_{ij}^{aH}, needed for the absorption coefficient, $\alpha_{\rm ec}$, is taken in the general integral formulation in the fully relativistic approach (see, e.g. [18]) for an arbitrary electron distribution function, f_e, (in the present calculations, the relativistic Maxwellian, $f_m = \frac{\mu}{2K_2(\mu)}\, e^{-\mu\gamma}$, with relativistic factor γ and $\mu = m_e c^2/T_e$). Performing the integration for ε_{ij}^{aH} in the variables $(\gamma, u_\parallel)$ with $u_\parallel = p_\parallel/mc$ as the dimensionless parallel momentum, the electron cyclotron absorption can finally be represented by the 1D integral,

$$\begin{aligned}\alpha_{\rm ec} &= -\frac{\pi\omega}{c\,|\mathbf{F}(\omega,\mathbf{N})|}\,\frac{\omega_{pl}^2}{\omega^2}\,\sum_n \int {\rm d}\gamma {\rm d}u_\parallel\;\delta\left(\gamma - \frac{n\omega_c}{\omega} - N_\parallel u_\parallel\right)\,\mathcal{D}_{ql}\,\hat{\mathcal{L}}(f_e) \\ &= -\frac{\pi\omega}{c\,|\mathbf{F}(\omega,\mathbf{N})|}\,\frac{\omega_{pl}^2}{\omega^2}\,\sum_n \int_{u_{\parallel min}}^{u_{\parallel max}} {\rm d}u_\parallel\;\left[\mathcal{D}_{ql}\,\hat{\mathcal{L}}(f_e)\right]_{\gamma=\gamma_{res}(u_\parallel)},\end{aligned} \tag{4}$$

where the limits of integration, $u_{\parallel min}$ and $u_{\parallel max}$, are defined from the resonance condition, $\gamma_{\rm res}(u_\parallel) = nY + N_\parallel u_\parallel$ with $Y = \omega_c/\omega$ as ratio of the cyclotron and wave frequencies, $\mathcal{D}_{ql} = u_\perp^2\,|\mathbf{\Pi}_n|^2$ is the normalized quasi-linear diffusion coefficient with the polarization factor $\mathbf{\Pi}_n = e_- J_{n-1}(k_\perp\rho_e) + e_+ J_{n+1}(k_\perp\rho_e) + e_\parallel\,(u_\parallel/u_\perp) J_n(k_\perp\rho_e)$, $k_\perp\rho_e = N_\perp u_\perp/Y$, and $\hat{\mathcal{L}} = \partial/\partial\gamma + N_\parallel\partial/\partial u_\parallel$ is the quasi-linear differential operator. Analyzing during integration along the resonance line the normalized magnetic momentum, $\lambda = p_\perp^2/p^2 b$ (here, $b = B/B_{\rm max}$ with $B_{\rm max}$ the maximum of the magnetic field, B, at the given flux surface), the absorption is decomposed into the contributions from trapped ($\lambda \geq 1$) and passing ($\lambda < 1$) electrons. Also the energy range of electrons responsible for absorption is calculated. The resonant harmonics, which may participate in cyclotron interaction, are defined automatically in the code by analyzing the magnetic configuration.

Similarly, the CD efficiency is calculated by applying the adjoint approach (see, e.g. Ref.[9]),

$$\eta = \frac{\langle j_\parallel\rangle}{P_{\rm abs}} = \frac{e v_{\rm th}\,\langle b\rangle}{\nu_{e0} m_e c^2}\,\frac{\sum_n \int_{u_{\parallel min}}^{u_{\parallel max}} {\rm d}u_\parallel\;\left[\mathcal{D}_{ql}\,\hat{\mathcal{L}}(f_e)\hat{\mathcal{L}}(\chi)\right]_{\gamma=\gamma_{res}}}{\sum_n \int_{u_{\parallel min}}^{u_{\parallel max}} {\rm d}u_\parallel\;\left[\mathcal{D}_{ql}\,\hat{\mathcal{L}}(f_e)\right]_{\gamma=\gamma_{res}}}, \tag{5}$$

where ν_{e0} is the (thermal) collision frequency and $v_{\rm th} = \sqrt{2T_e/m_e}$. The response (Green's) function, $\chi(u,\lambda)$, is defined here with trapped electrons taken into account, i.e. in the low-collisionality limit where the bounce frequency for all electrons is assumed to be much larger than their collision frequency, $\omega_b(u,\lambda) \gg \nu_e(u)$,

$$\begin{aligned}&\chi(u,\lambda) = -{\rm sign}(u_\parallel)\,H(\lambda)\,F(u), \\ &H(\lambda) = \frac{1}{2}\Theta(1-\lambda)\int_\lambda^1 \frac{{\rm d}\lambda}{\left\langle\sqrt{1-\lambda b}\right\rangle},\end{aligned} \tag{6}$$

where $\Theta(x) = 1$ for $x \geq 0$ (passing particles), and $\Theta(x) = 0$ for $x < 0$ (trapped particles), $F(u)$ is the Spitzer function, and $\langle ...\rangle$ denotes flux surface averaging.

Since the mc-model for the Spitzer function is the more general one (and includes as a limit the hsl-model), this model is defined as standard in the TRAVIS code for calculations of current drive. The formulation of the mc-model is taken from [10], where the linearized collision operator in the non-relativistic approach was applied. In fact, the model [10] is easily adapted to the relativistic formulation by substituting $v/v_{\rm th} \approx p/p_{\rm th}$, since the asymptotic behavior of the Spitzer function, $F(u)$, for $u \gg 1$ is the same for both relativistic and non-relativistic cases. Apart from this, the hsl-model can also be applied as the reference model. In this case, the hsl-model can be applied in two forms: i) the standard formulation proposed in [9], and ii) the asymptotic formulation given in [8].

The TRAVIS code has been benchmarked against the old W7-AS code [10], the code WR_RTC [19] and the code TORBEAM [20]. Additionally, the code was successfully tested on the ITER reference Scenario-2 [15] against several other predictions collected by R. Prater [6, 7] (the results of this benchmark are not included in the cited papers). As expected, although all data such as trajectory, absorption, deposition profile, etc., perfectly coincide with the results obtained by other codes, the current drive efficiency is the same only for the asymptotic form of the hsl-model (Cohen-like model).

The code is now routinely exploited in modeling heating at various harmonics of the ordinary and extraordinary mode (O1, O2, X2 and X3) in different W7-X magnetic configurations. The code is also used to support the design of ECRH launcher components for the W7-X stellarator [21].

3. Optimal angles for the upper launcher

For suppressing the NTM, the RF beam from the upper launcher must be absorbed at the magnetic surfaces $q = 3/2$ and $q = 2$. The launch angles are defined in such a way, that the ECCD efficiency should be maximum there and should have a high localization of the driven current. The Gaussian beam with divergence of 1.08° starts from the point ($R = 6.485$ m, $Z = 4.11$ m) with the initial width 9.43 mm (which corresponds to the wave-front radius 0.5 m). The ITER launching angles, α and β, are defined as $\alpha = -\tan^{-1}(N_Z/N_R)$ and $\beta = \sin^{-1}(N_\phi)$, where (N_R, N_ϕ, N_Z) is the central ray unit vector in cylindrical coordinates, (R, ϕ, Z). The sign of the current drive is defined as positive if it coincides with the plasma current. Since the ITER toroidal magnetic field is directed clockwise, the current drive is normally positive for the angles $\beta > 0$ and, consequently, $N_\parallel < 0$.

For comparison, in Fig. 1 the ECCD efficiencies are shown, calculated with the hsl-model (left) and mc-model (right). The locations of the driven current as a function of the launch angles are also shown (for simplicity, only the two most interesting lines are shown, $\rho = 0.65$ and $\rho = 0.77$, which correspond to the $q = 3/2$ and $q = 2$ magnetic surfaces, respectively). As expected, the ECCD locations (and the width of the current profile) are almost completely defined by the deposition profile and coincide for both models with high accuracy. However, the current drive values obtained by the

different models are not the same. First, the maximum of the efficiency calculated by the mc-model is visibly shifted into the region of smaller toroidal angles. Moreover, the (toroidal) angle dependence is not so peaked as calculated with the hsl-model, and this circumstance is very positive from the point of view of sensitivity of the launcher against errors in direction.

For some angles the efficiencies obtained by these models are significantly different, up to a factor of two. The difference is most pronounced in the range of small toroidal angles. For example, for $\alpha = -70°$ and $\beta = 10°$, the RF power is completely absorbed by the electrons with $p_{\rm res}/p_{\rm th} < 1$, where the applicability of the hsl-model brakes down and momentum conservation is important. Nevertheless, these angles are outside the normal conditions for operation of the upper launcher. The maximum of the ECCD efficiency in the most interesting region, i.e. where the power is deposited near the desired magnetic surfaces, is not so different for hsl- and mc-models.

The optimal launch angles have to correspond to the maximum of the current drive density near the desired magnetic surface. For deposition, say, at the $q = 3/2$ surface, the mc-model predicts the optimal launch angles $\alpha^{\rm mc} \approx -61°$ and $\beta^{\rm mc} \approx 18°$, which are somewhat different from the preliminary choice, $\alpha^{\rm hsl} \approx -63.5°$ and $\beta^{\rm hsl} \approx 22°$, made from calculations by the code with the hsl-model [6]. Comparing the angle scan results for both models (Fig. 2), one can see, that the maximum of the ECCD predicted by the mc-model has significantly smoothed angle dependence, similar to Fig. 1. As a consequence, the choice of the optimal angles seems to be not so strict as predicted by the hsl-model.

The influence of the parasitic 2nd harmonic is also checked, and its contribution is found to be negligible for the upper launcher for the angles belonging to the main range of interest. The last conclusion is in agreement with [22], where the absorption at the 2nd harmonic was found to be important (and even dominating) only for such large poloidal angles (quasi-vertical launch), that the main resonance cannot be reached due to refraction effects.

4. Angle scanning for the equatorial launcher

The mirrors of the equatorial launcher have a fixed angle for the vertical direction, $\alpha = 0$, and only the toroidal angle β can be used for ECCD. The beam properties are taken the same as for the upper launcher, i.e. Gaussian shape with divergence of 1.08° and the initial width 9.43 mm. In Fig. 3, ray-tracing results from one starting position, ($R = 9.076$ m, $Z = 1.211$ m), i.e. from the top mirror of the equatorial launcher, are presented. The main tendency of the angle dependence for ECCD efficiency (Fig. 3, left) is similar to that obtained for the upper launcher: while for large angles the ECCD efficiencies calculated by both models are quite similar (with a discrepancy of about 20%), for small angles the difference is significantly larger (up to a factor of about two). This difference is the direct consequence of the different energies of resonant electrons. Due to significant Doppler shift for the large angles, the supra-thermal

electrons are mainly responsible for driving the current, while for the opposite case the bulk electrons are involved in cyclotron interaction, where momentum conservation produces a significant correction to the current.

Apart from the ECCD efficiency, the factors $I_{cd}/\Delta\rho$ (not shown here) and $I_{cd}/\Delta\rho^2$ are also important for the choice of the launch angles [1] ($\Delta\rho$ is the width of the ECCD profile with ρ as the normalized effective radius). Here, $I_{cd}/\Delta\rho^2$ is the figure of merit for both the NTM stabilization [23] and the sawtooth period control [24]. Comparison of the results shown in Fig. 3 on the right, gives the following: the angle dependence obtained by the mc-model is less peaked than predicted by the hsl-model. Due to the coincidence of the peaks of I_{cd} and $I_{cd}/\Delta\rho^2$, the launch with angles $\beta \approx 22^\circ$ seems most favorable for driving current, while for larger angles $I_{cd}/\Delta\rho^2$ drops rapidly due to significant Doppler broadening. The location and the width of the current drive profile (Fig. 4) coincide well with the results of [3] (with appropriate inversion of the toroidal angle sign). Since these values are defined (almost completely) by the deposition profile characteristics, the results for hsl- and mc-model coincide with high accuracy.

In principle, the cyclotron interaction at the parasitic higher (2nd) harmonic may lead to the appearance of a counter-current [8, 12], but for the present scenario the influence of this effect was found to be important neither for absorption (usually, not more than 5% of the power is "lost") nor for the current drive (see Fig. 3). On the other hand, as was indicated by Fokker-Planck simulations in [25, 26], for some conditions the Ohkawa effect [27] can produce (at least) a non-negligible contribution to the total current. Nevertheless, for the present scenario, the fraction of power absorbed by trapped electrons (being a non-direct weight-factor for the Ohkawa effect) is negligibly small, and the Ohkawa current is not expected to be important.

5. Scenario with reduced magnetic field

The scenario with somewhat reduced magnetic field may significantly improve the ability of the upper launcher for creating highly peaked ECCD [3, 4]. However, due to the absorption at the parasitic higher harmonic, which is expected to be much more pronounced compared with the nominal magnetic field, this scenario may be very unfavorable for the equatorial launcher.

Holding constant the safety factor, q, pressure, $\beta_{\rm pol}$, and collisionality, ν^*, (the alternative scaling, that based on the Greenwald density limit instead of collisionality, is not considered in this paper), the plasma profiles are scaled as [4] $n_e = g^{4/3} n_e^{Sc2}$ and $T_e = g^{2/3} T_e^{Sc2}$ with the scale-factor, g, defined by $B = gB^{Sc2}$ (here, n_e^{Sc2} and T_e^{Sc2} correspond to the reference Scenario-2 with the nominal magnetic field $B^{Sc2} = 5.3$ T). Let us consider the case with $B = 4.5$ T (consequently, $g \simeq 0.85$), when the 1st harmonic resonance is shifted to the high-field-side. In Fig. 5, the results of scanning over the toroidal launch angle (similar to Fig. 3) are presented. One can see that, contrary to the case of nominal (non-reduced) magnetic field, the ECCD efficiencies (Fig. 5, left) with only the 1st harmonic taken into account coincide well for both the hsl- and mc-model in

the small-angle range. It is a consequence of the increased fraction of trapped electrons on the periphery, where the power deposited, and the friction over the trapped electrons masks the correction of ECCD due to momentum conservation. Conversely, for large launch angles, 1st harmonic absorption is located close to the axis, where momentum conservation correction is significant. As a result, the ECCD efficiency predicted by the mc-model for large angles differs from the hsl-model by about 25%. It must also be mentioned that (similar to the case with nominal magnetic field) the location and the width of the current profile are almost the same as shown in [3] when only the 1st harmonic is taken into account. In the case when $n = 2$ is included, the current drive profile as well as the deposition profile at small toroidal angles loses its locality and becomes broader for large angles. Comparing the ECCD efficiency calculated by the mc-model for both $n = 1$ and $n = 1, 2$ cases, one can conclude that the influence of the parasitic harmonic almost disappears only for the large launch angles, where an overlap of the location for both harmonics appears with dominating absorption at the main harmonic. This can be seen in Fig. 6, where (similar to the Fig. 4) the location of $j_{\parallel,\max}$ with the width of the current profile for both harmonics is shown. As a consequence, the contributions from $n = 1$ and $n = 2$ become undistinguishable and the absorption at $n = 1$ is dominant.

As already discussed above, the reduction of the total current drive happens due to the counter-current, which appears at the down-shifted 2nd harmonic resonance, and this effect is much more pronounced in the present case of reduced magnetic field. Indeed, the increase of B along the beam trajectory from the low-field side is compensated by the increase of T_e, and the resonance may appear for nearly bulk (thermal) electrons. To illustrate this, in Fig. 7 the optical depth (left) and the normalized momentum of the electrons responsible for cyclotron interaction (right) are shown as functions of the path along the central ray trajectory launched with the angle $\beta = 10^\circ$. This angle corresponds to the range with significant influence of the parasitic cyclotron interaction. The main absorption at the 2nd harmonic happens when the ray passes through the plasma core where T_e is high enough and $p_{\rm res}/p_{\rm th} \sim 2 - 3$ (Fig. 7, right). In this case, the increasing of B along the ray is compensated by increasing the temperature, T_e and parallel refractive index, $N_\parallel$, leading to a reduction of energy for the resonant electrons almost up to the thermal range. In principle, this interaction is rather weak, but due to the long path in the hot plasma the integral effect becomes significant: the optical depth for the unwanted $n = 2$ resonance reaches the value of about 0.4 (Fig. 7, left), and approximately 25% of the power is absorbed much before the desired resonance. The point where the desired resonance ($n = 1$) is reached corresponds to the jump of the resonant momentum to the thermal value, $p_{\rm res}/p_{\rm th} \sim 1 - 2$, and the optical depth is sharply increased there, indicating complete absorption. The resulting deposition and ECCD profiles for this case are shown in Fig. 8. The sharp peak of the desired $n = 1$ contribution is located near $\rho = 0.58$, while the $n = 2$ contribution is distributed over the inner volume, $0.12 < \rho < 0.4$ (in Fig. 7, it corresponds approximately to the part of the trajectory beyond 4.2 m for

$n = 1$, and to the area between 2 m and 3 m for $n = 2$). The shape of the ECCD profile tracks quite well the shape of the deposition profile (for passing electrons), but with the inverted contribution from the 2nd harmonic, which is comparable with the main one. The counter-current from the 2nd harmonic is about 70% of the total current ($I_{cd}^{n=1} \simeq 5.1$ kA and $I_{cd}^{n=2} \simeq -2.1$ kA, obtained for $P_{RF} = 1$ MW). An inversion of $I_{cd}^{n=2}$ happens due to the dominating contribution of the electrons with $k_\parallel v_\parallel < 0$. The power absorbed by the trapped electrons does not exceed 3% (Fig. 8, left, dashed line), and, consequently, the Ohkawa effect is negligible for this case.

The influence of the parasitic harmonic may even drastically change the scenario for the equatorial middle mirror, the beam from which passes near the axis. Its effect becomes small only for the highest launch angles, $\beta > 25°$. For the small angles, $\beta < 10°$, the power losses at the parasitic 2nd harmonic can reach 35% with predominantly counter-current drive.

6. Summary

The ECCD efficiency for the ITER upper launcher as well as for the equatorial launcher (top mirror) was calculated by two models, with and without parallel momentum conservation. For the upper launcher, it has been shown, that the angle dependence calculated with the mc-model is less peaked than that obtained with the hsl-model. The expected optimal launch angles do not coincide with the previous predictions, being somewhat shifted in the direction of smaller angles, and should be revised carefully. For example, it seems reasonable to accept the optimal toroidal angle for the upper launcher as $\beta_{\rm opt} \simeq 18°$ instead of $\beta_{\rm opt} \simeq 22°$, which was obtained from the hsl-model.

In the case of reduced magnetic field, additional care is needed for taking into account the higher parasitic harmonic which may be important for the ECCD profile (especially for the equatorial launcher). In particular, for $B = 4.5$ T (with the plasma parameters from Scenario-2, but scaled in a proper way) a significant part of the power can be absorbed (up to 25% for the top mirror and up to 35% for the middle mirror of the equatorial launcher) much before the desired resonance $n = 1$ is reached, and the current contribution driven due to the parasitic 2nd harmonic has the opposite sign. The trapped electrons are only slightly involved in the cyclotron interaction, and the Ohkawa effect is negligible. As a consequence, a launch of power under small toroidal angles, $\beta < 15°$, is not only non-optimal for high efficiency, but loses locality of the heating. It is easy to check also, that for the half-field scenario, $B = 2.65$ T, (not included in this paper) only the ordinary mode with 2nd harmonic absorption is applicable for ECCD production with help of the equatorial launcher, while the extra-ordinary mode is absorbed almost completely (more than 90%) at the 3rd harmonic mainly by trapped electrons far before the 2nd harmonic is reached.

Acknowledgments

The authors wish to thank Volker Erckmann for fruitful discussions, and Ron Prater for providing the ITER Scenario-2 data files.

References

[1] H. Zohm *et al* 2007 *Nuclear Fusion* **47** 228
[2] H. Zohm 2004 Proc. of 13th Joint Workshop on Electron Cyclotron Emission and Electron Cyclotron Heating, Nizhny Novgorod, Russia, May 17-20, 2004, p.133, http://www.ec13.iapras.ru
[3] R. Prater 2005 *Journal of Physics: Conf. Series* **25** 257
[4] G. Ramponi, D. Farina, S. Nowak 2005 *Journal of Physics: Conf. Series* **25** 243
[5] R. Prater *et al* 2003 Proc. of IAEA TM on ECRH physics and technology, Closter Seeon, Germany (2003) http://www.ipp.mpg.de/tmseeon
[6] R. Prater *et al* 2006 Proc. of 14th Joint Workshop on Electron Cyclotron Emission and Electron Cyclotron Heating, Santorini, Greece (2006) http://www.hellasfusion.gr/ec14/papers/37.pdf
[7] R. Prater *et al Nuclear Fusion* **48** 035006
[8] R.H. Cohen 1987 *Phys. Fluids* **30** 2442
[9] Y.R. Lin-Liu, V.S. Chan and R. Prater 2003 *Phys. Plasmas* **10** 4064
[10] M. Romé *et al* 1998 *Plasma Phys. Control. Fusion* **40** 511
[11] S.P. Hirshman 1980 *Phys. Fluids* **23** 1238
[12] M. Taguchi 1989 *Plasma Phys. Control. Fusion* **31** 241
[13] N.B. Marushchenko *et al* 2006 Proc. of 14th Joint Workshop Electron Cyclotron Emission and Electron Cyclotron Heating, Santorini, Greece, May 9-12, 2006, http://www.hellasfusion.gr/ec14/papers/26.pdf
[14] N.B. Marushchenko *et al* 2006 Proc. of 16th Toki Conference, Toki, Japan, December 5-8, 2006, http://itc.nifs.ac.jp/index.html
[15] Y. Gribov, Plasma of ITER Scenario 2, Issue 4: 31 March 2005
[16] E. Mazzucato 1989 *Phys. Fluids B* **1** 1855
[17] M.D. Tokman, E. Westerhof and M.A. Gavrilova 2000 *Plasma Phys. Control. Fusion* **42** 91
[18] M. Bornatici *et al* 1983 *Nucl. Fusion* **23** 1153
[19] M.A. Balakina, M.D. Tokman and O.B. Smoliakova 2003 *Plasma Phys. Reports* **29** 53
[20] E. Poli, A.G. Peeters, G.V. Pereverzev, Comp. Phys. Comm. **136** 90 (2001)
[21] V. Erckmann *et al* 2007 *Fusion Sci. Technol.* **52** 291
[22] H. Bindslev 2004 *Nucl. Fusion* **44** 731
[23] A. Pletzer and F.W. Perkins 1999 *Phys. Plasmas* **6** 1589
[24] A. Merkulov *et al* 2004 Joint Varenna-Lausanne Intern. Workshop on Theory of Fusiion Plasmas, Varenna, Italy, August 30 - September 3, 2004, p.279
[25] B. Lloyd *et al* 2002 Proc. of 12th Joint Workshop on Electron Cyclotron Emission and Electron Cyclotron Heating, Aix-en-Provence, France, May 13 - 16, 2002, http://wshop.free.fr/ec12/PAPERS/072-Lloyd.pdf
[26] F. Volpe 2005 *Journal of Physics: Conf. Series* **25** 283
[27] T. Ohkawa 1976 "Steady State Operation of Tokamaks by R-F Heating", General Atomics Report GA-A13847.

LIST OF FIGURE CAPTIONS

Figure 1: Upper launcher: current drive efficiency isolines for both hsl-model (left) and mc-model (right) as functions of the poloidal and toroidal launch angles (α and β, respectively) are shown. Thick lines indicate the angles where the current drive is located on the surfaces $q = 3/2$ and $q = 2$. The optimal launch angles are by circles marked.

Figure 2: Upper launcher: maximum of the current drive for both hsl-model (left) and mc-model (right). Notations are the same as in Fig. 1.

Figure 3: Launch from the equatorial top mirror: ECCD efficiency, I_{cd}/P_{RF} (left), and its (normalized) density, $I_{cd}/(P_{RF}\Delta\rho^2)$ (right), for both hsl-model (triangles) and mc-model (circles) are shown. For comparison, calculations are performed with the $n = 1$ harmonic (dashed lines) as well with the $n = 1, 2$ harmonics (full lines) taken into account.

Figure 4: Launch from the equatorial top mirror: The location of $j_{\parallel,\max}$ with the width of the current profile shown by the bars.

Figure 5: Reduced magnetic field, $B = 4.5$ T, launch from the equatorial top mirror: the same as in Fig. 3.

Figure 6: Reduced magnetic field, $B = 4.5$ T, launch from the equatorial top mirror: The same as in Fig. 4 for both harmonics, $n = 1$ and $n = 2$ (location of $n = 2$ contribution is shown only for the angles where no overlapping occurs with $n = 1$).

Figure 7: Reduced magnetic field, $B = 4.5$ T, launch from the equatorial top mirror with $\alpha = 0°$ and $\beta = 10°$: optical depth τ (left) and the resonance momentum range (right). Note, that the full line in the $p_{\rm res}/p_{\rm th}$ picture indicates the values which correspond to the maximum of absorption in momentum space (here, $p_{\rm th} = \sqrt{2m_eT_e}$).

Figure 8: Reduced magnetic field, $B = 4.5$ T, launch from the equatorial top mirror with $\alpha = 0°$ and $\beta = 10°$: deposition (left) and ECCD profiles (right). Besides the total deposition, (full red line), also the contributions from the passing (blue dash-dot) and trapped particles (green dash) are shown.

Figure 1

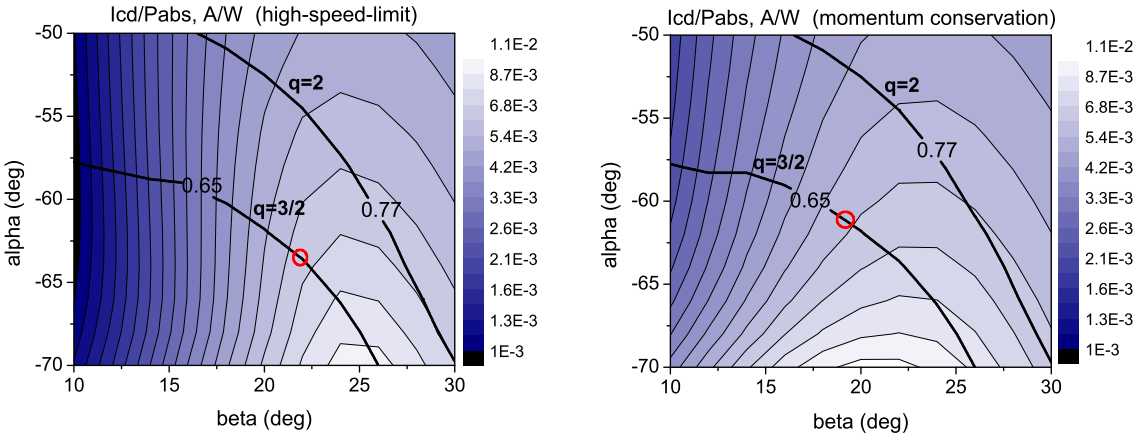
Icd/Pabs, A/W (high-speed-limit)
Icd/Pabs, A/W (momentum conservation)
alpha (deg)
beta (deg)
-50
-55
-60
-65
-70
10
15
20
25
30
q=2
q=3/2
0.65
0.77
1.1E-2
8.7E-3
6.8E-3
5.4E-3
4.2E-3
3.3E-3
2.6E-3
2.1E-3
1.6E-3
1.3E-3
1E-3

Figure 2

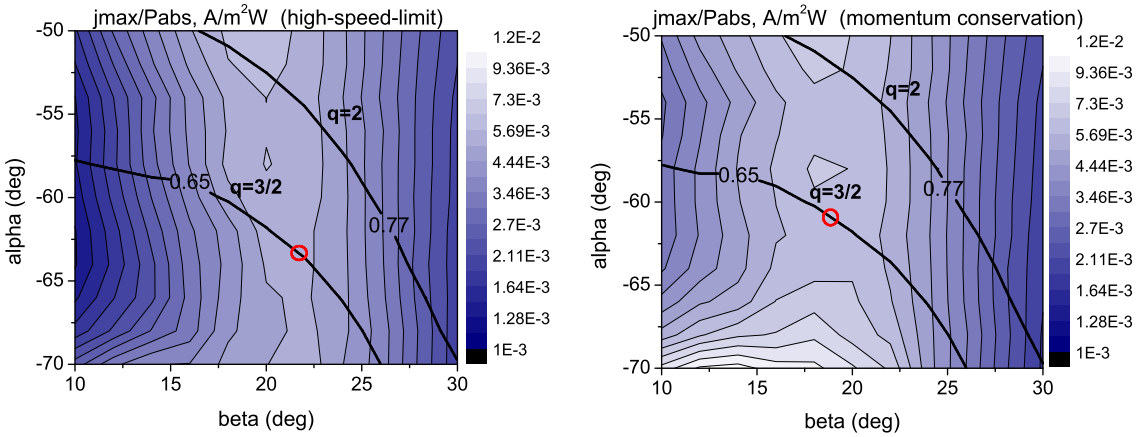
jmax/Pabs, A/m^{2}W (high-speed-limit)
jmax/Pabs, A/m^{2}W (momentum conservation)
alpha (deg)
beta (deg)
-50
-55
-60
-65
-70
10
15
20
25
30
q=2
q=3/2
0.65
0.77
1.2E-2
9.36E-3
7.3E-3
5.69E-3
4.44E-3
3.46E-3
2.7E-3
2.11E-3
1.64E-3
1.28E-3
1E-3

Figure 3

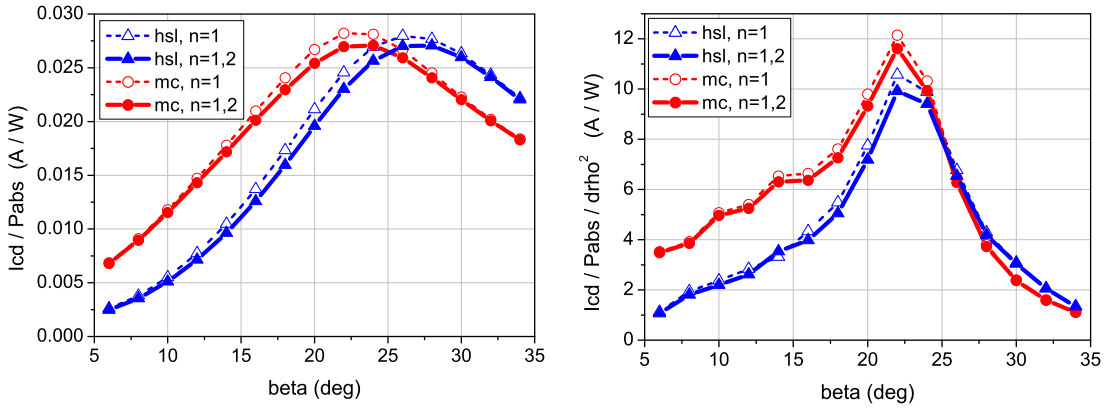
hsl, n=1
hsl, n=1,2
mc, n=1
mc, n=1,2
Icd / Pabs (A / W)
beta (deg)
Icd / Pabs / drho^2 (A / W)
beta (deg)

Figure 4

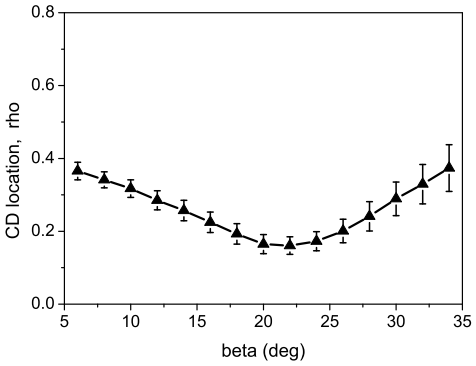

Figure 5

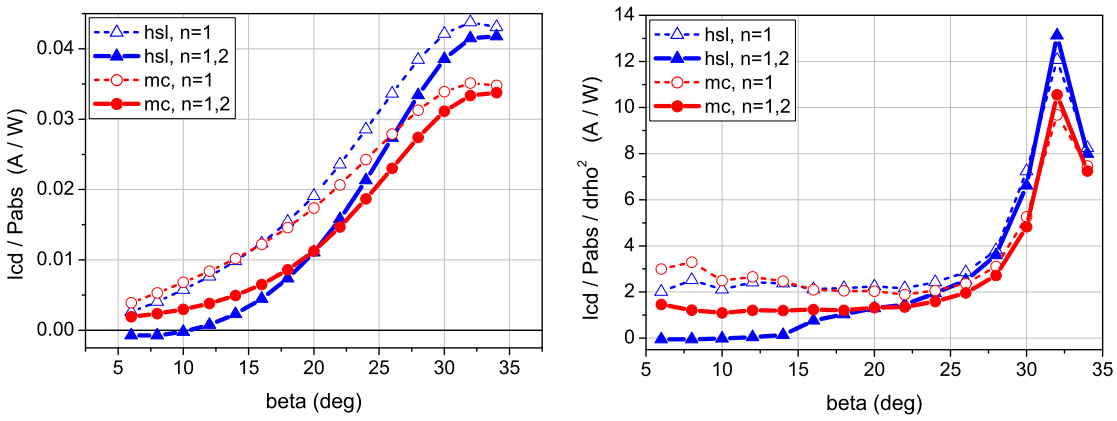
hsl, n=1
hsl, n=1,2
mc, n=1
mc, n=1,2
Icd / Pabs (A / W)
beta (deg)
Icd / Pabs / drho^2 (A / W)
beta (deg)

Figure 6

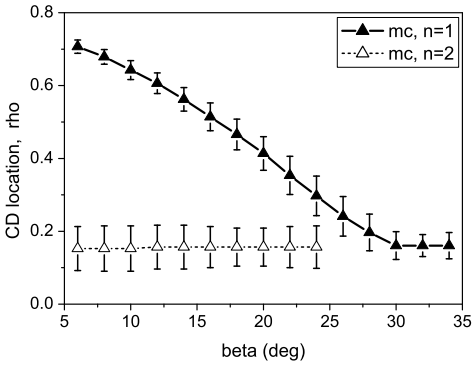
mc, n=1
mc, n=2
CD location, rho
beta (deg)
0.0
0.2
0.4
0.6
0.8
5
10
15
20
25
30
35

Figure 7

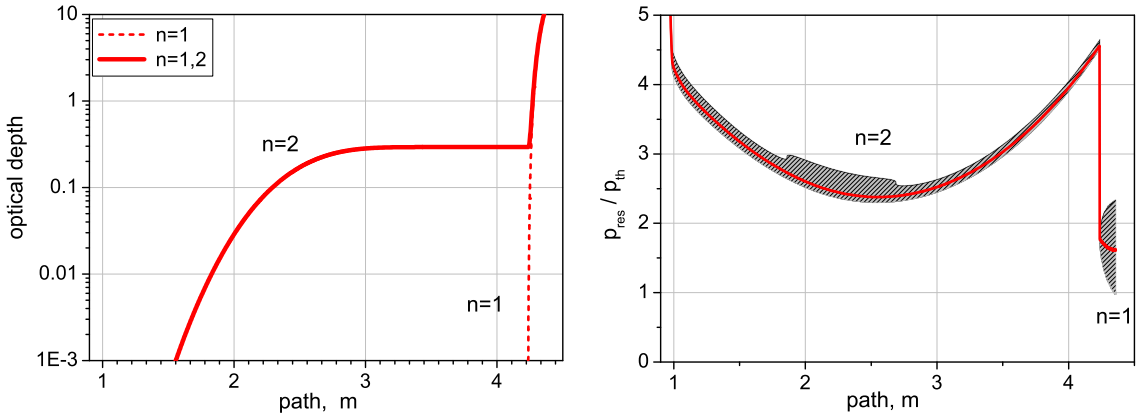
n=1
n=1,2
optical depth
10
1
0.1
0.01
1E-3
n=2
n=1
1
2
3
4
path, m
p_{res} / p_{th}
5
4
3
2
1
0
n=2
n=1
1
2
3
4
path, m

Figure 8